Article

Influence of Plasma on the Combustion Mode in a Scramjet

Yu Meng [1,2], Hongbin Gu [2,*] and Fang Chen [1]

1   School of Aeronautics and Astronautics, Shanghai Jiao Tong University, Shanghai 200240, China; yumeng123@sjtu.edu.cn (Y.M.); fangchen@sjtu.edu.cn (F.C.)
2   Institute of Mechanics, Chinese Academy of Sciences, Beijing 100190, China
*   Correspondence: guhb@imech.ac.cn

Abstract: To examine the plasma-assisted combustion of a scramjet, a microwave-enhanced gliding arc plasma method was proposed in this study, and the flame structure and combustion instability were observed. The mechanism of plasma-assisted combustion was obtained via a Bunsen experiment, and then the influence on supersonic combustion was obtained on a direct-connected scramjet. The active species of the flame was determined via optical emission spectroscopy, and the flame temperature was measured with a thermocouple. The luminous intensity of the OH radicals in the flame increased ninefold when the flame temperature was increased to 1573 K, but the luminous intensity of CH* and C_2 was not obviously changed with the excitation of arc plasma. Moreover, the DC arc plasma had no effect on the rotation and the vibration temperature of OH radicals under these experimental conditions. In the range of microwave energy less than 800 W, there was no typical change in the intensity of the radicals; however, when the microwave power was up to 1000 W, the effect became obvious. When plasma was applied to the scramjet, the plasma caused the pre-combustion shock train to move forward, and the initial and stable position of the flame was transferred from the cavity shear layer to the front of the fuel jet. These results clearly show that plasma free radical mechanisms cause changes to combustion modes.

Keywords: scramjet; combustion; plasma; microwave

1. Introduction

Ignition and flame stabilization is challenging work in a scramjet [1–3]. The residence time of air in a combustor ($t_{\text{flow}} \approx 0.5$ ms) is even shorter than the typical self-ignition time of fuel ($t_{\text{ig}} \approx 1$–2 ms) [4–6]. Traditional passive flame stabilization methods (such as cavity and plate flame stabilization) stabilize a flame in a vortex structure to achieve the purpose of stable combustion, which is dominated by supersonic inflow and formed passively. The interaction between the instability of the inflow and the combustion affects the flame structure [7–11]. Especially in the process of acceleration, it has been pointed out that the combustor inlet flow acceleration will lead to the transition of the flame mode [12,13]. Therefore, a more effective flame stabilization method is needed in order to stabilize flames actively so that the flame structure can be accurately controlled.

Plasma is an important way to assist combustion, which can improve cycle efficiency in internal combustion engines and turbines [14–16]. Since plasma produces heat, electrons, long-lifetime intermediate species, radicals, ions, excited molecules, fuel fragments, ionic wind, a large density gradient, and Coulomb and Lorentz forces, it mainly affects combustion via three different pathways: thermal, kinetic, and transport (including aerodynamic) [17–19]. In fact, the three effects often exist at the same time. Recent studies using torch plasma, filamentary discharge, microwave discharge, low-frequency arc discharge, streamer high-frequency (HF) discharges, surface discharges, and nanosecond pulsed discharges (NSDs) [20] have shown that plasma can enhance ignition, flame stabilization, and fuel/air mixing via chemical, thermal, and plasma-induced aerodynamic effects [21–24].

In 2013, Yu et al. [25] successfully used 1.5 kW torch plasma to ignite liquid kerosene in a scramjet, with a Mach number of 1.8 and a total temperature of 950 K. Sun et al. [26] studied flame stabilization with a spark discharge. Li et al. [27] achieved scramjet ignition and flame stabilization by using a gliding arc in a cavity, and extended the lean ignition limit by 17%.

However, a plasma torch or arc plasma can only generate plasma in a single position, and cannot form the effect with full-field combustion. Compared with the plasma formed by a high-voltage discharge, the process of microwaves forming plasma is more complicated. The electric and magnetic fields of microwaves accelerate the electrons, and the microwaves also increase the vibrational energy of the chemical bonds of molecules. The influence of microwaves is regional, so it may be more efficient to use microwaves to enhance combustion kinetics.

Jaggers et al. [28] explained the mechanism of using an electric field to increase the premixed flame velocity. An electric field acts on the free electrons in a flame, causing the combustion reaction rate to increase. Shinohara et al. [29] used 2.45 GHz microwaves to increase the flame velocity, and determined that the microwave electromagnetic field enhanced the non-equilibrium plasma concentration.

Stockman [30–32] and Khodataev [33] suggested that the subcritical discharge characteristics of microwaves in high-pressure gas could be applied to a scramjet combustor. The microwave critical discharge zone could be used as a flame holder without a cavity or other geometric flame-stabilizing structure to avoid the problem of high heat flux [34–37].

However, there is a wall effect in microwave critical discharge that is detrimental to combustion and wall cooling. A new full-field plasma-assisted combustion method is required. The composite plasma can discharge in a large area, which is an ideal method of combustion assistance, such as for a double-pulse laser [38], microwave-enhanced laser, or spark plasma [39].

Michael et al. [39] used microwaves to enhance laser plasma, and achieved dynamic characteristics that showed that microwaves had an expanding effect on the plasma and could produce a larger volume of plasma. Ikeda et al. [40,41] developed a microwave-enhanced spark-discharge plasma generation method, and the microwaves expanded the spark plasma. Elsabbagh et al. [42] suggested that microwaves could enhance the rotation temperature of N_2 excited in the plasma and increase the number of ion groups in the plasma significantly. At present, microwave-enhanced spark-discharge plasma ignition has been widely studied in internal combustion engines [2].

In this study, a method of microwave-enhanced gliding-arc-plasma-assisted combustion was proposed and applied to a scramjet. Gliding arc plasma is a kind of arc that is extended and elongated with the action of air flow, and it has the characteristics of a mixture of equilibrium and non-equilibrium gas [43]. Compared with spark-discharge and laser plasma, it has the advantage of a larger area, and is easy to achieve. After microwave expansion, a gliding arc can achieve plasma distribution in a larger volume to assist combustion.

2. Materials and Methods

The experiment included two parts: a Bunsen experiment and a scramjet experiment, corresponding to mechanism verification and the application of assisted supersonic combustion, respectively. The first part was carried out using a Bunsen burner, and the second part was carried out on a direct-connected scramjet model.

2.1. Experimental Setup on a Bunsen Burner

Figures 1 and 2 display a schematic diagram and the real setup of the experiment, respectively. The premixed gas contained ethylene and air with a suitable equivalence ratio, precisely controlled by calibrated "Ω" float flowmeters, while the pipelines and mix chamber ensured that the gases were sufficiently mixed.
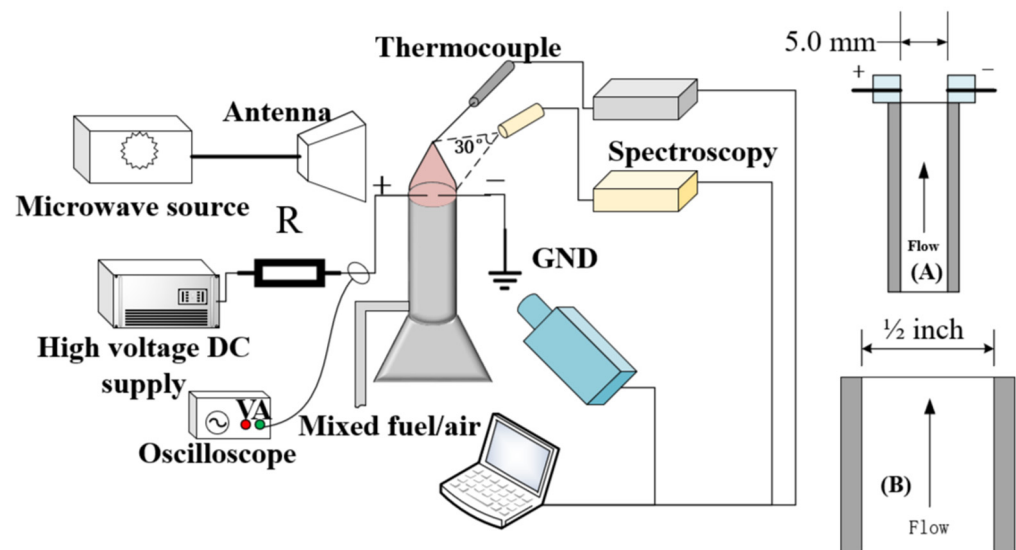
Figure 1. Experimental setup of the Bunsen system: (**A**) Bunsen burner A for experiment HV; (**B**) Bunsen burner B for experiment MW.
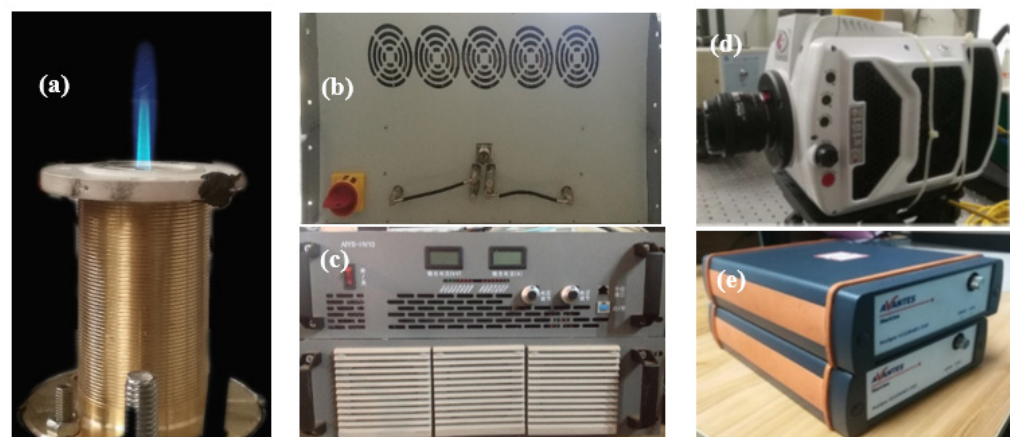

Figure 2. Real setup of the Bunsen experimental system: (**a**) Bunsen burner; (**b**) microwave source; (**c**) high-voltage power supply; (**d**) high-speed camera; (**e**) optical emission spectroscopy.

The high voltage (HV) used for discharging was supplied by an HV DC supplier with a maximum power of 10.0 kW, a maximum voltage of 10.0 kV, and a maximum current of 1.0 A, and the arc discharge was monitored by an HV probe combined with a digitizing oscilloscope.

The microwaves were produced by a microwave source. The maximum continuous output power of the microwave source was 1000 W, and the maximum peak pulse output power was 2000 W, while the maximum duty cycle was 50%. The microwaves were emitted by the horn antenna and acted directly on the flame. The microwave source and the antenna were connected by a coaxial line. The working mode of the arc and that of the microwaves were set to work separately, and not to be turned on at the same time.

The Bunsen burners used in this study are shown in Figure 1A,B. Bunsen burner A (Figure 1A) was a ceramic tube with an internal diameter of 5 mm, and corresponded to the experiment Case HV in Table 1. The two tungsten electrode needles (diameter of 1 mm) were arranged 2 mm inside the tube outlet (Figure 1A). The Bunsen burner was isolated from the environment. Between the HV DC supply and the Bunsen burner were protection resistors that protected the power supplier. Bunsen burner B (Figure 1B) was a metal tube with an internal diameter of 1/2 inch, corresponding to experiment Case MW in Table 2.

Table 1. Experimental parameters of HV (high voltage).

Case	C_2H_4 Flow (L/min)	Air Flow (L/min)	Equivalence Ratio	Arc Power (W)
HV	0.05	7.2	1	off 32.85 37.93 42.89 49.52 56.27 70.85

Table 2. Experimental parameters of MW (Microwave).

Case	Flow Velocity (m/s)	Flow (L/min)	Equivalence Ratio	Microwave Power (W)
MW	0.5	3.80	0.6	off 100 300 500 800 1000

Optical emission spectroscopy (Avantes, Apeldoorn, the Netherlands) measurement was employed to determine the active species of the flame. The Avantes spectrometer probes were placed at a fixed distance from the flame to capture the entire flame emission. The K-type thermocouple was used to measure the temperature of the flame. The thermocouple was inserted into a fixed position of the flame, as shown in Figure 1. Temperature and spectral measurements were taken at different times for the same operating conditions.

The HV experiment case is shown in Table 1; Case HV included seven arc power cases. The MW experiment case is shown in Table 2; Case MW included six microwave power cases.

2.2. Discharge Characteristics of the DC Arc in the Bunsen Burner

This section gives the characteristics of the arc in the flame. As shown in Figure 3, the flame temperature rose significantly after the arc was added, but it did not always increase with the increase in the arc power, and did increase with the arc current I. The power represented the heat release of the arc, and the current represented the transport rate of charged particles in the arc. Since plasma-assisted combustion has both thermal and non-equilibrium effects, it could be concluded that the influence of the DC arc resulted in thermal and ionic enhancement.

2.3. Experimental Setup of the Scramjet Experiment

Plasma-assisted supersonic combustion experiments were conducted on the direct-connected supersonic combustor, as shown in Figure 4. The heater combusted air, hydrogen, and oxygen, and after combustion, the oxygen molar fraction was 21%. The combustor inlet's total temperature and flowrate were controlled by the hydrogen, oxygen, and air flowrates. The data were acquired using an automated control and data acquisition system. For this study, the Mach number of the combustor inlet flow was 2.5, the total temperature was 1249 K, the total pressure was 1.55 MPa, and the total flowrate was 1.77 kg/s.

The experimental combustor model had a rectangular cross-section with one side expansion, an expansion angle of 2°, an inlet height of 40 mm, and a width of 80 mm. A single cavity was used to stabilize the flame. On the opposite side of the cavity, a horn antenna was used to feed 2.45 GHz microwaves. The structure of the model is shown in Figure 5a.
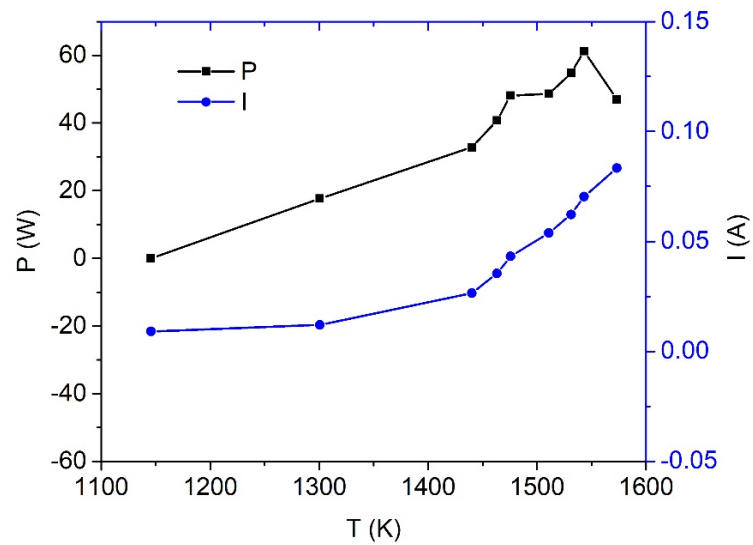
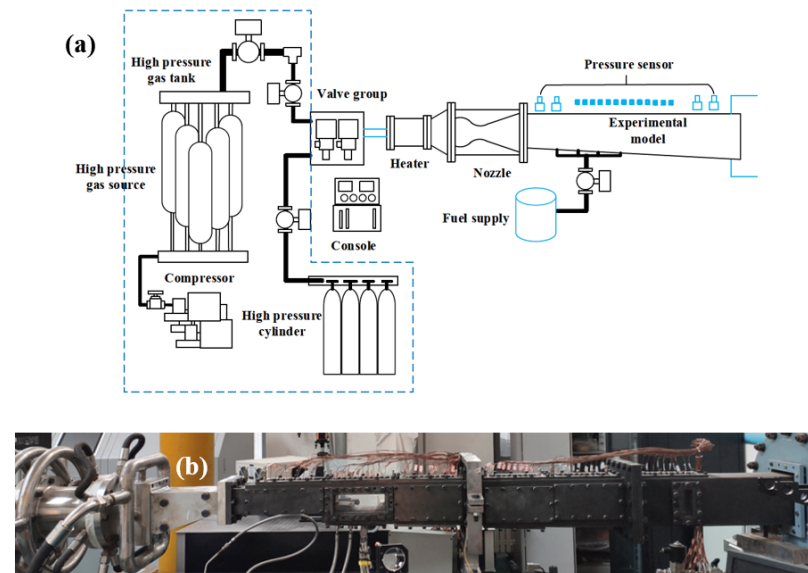**Figure 3.** Flame temperature versus arc power P and current I.

Figure 4. Supersonic combustor experimental system, (**a**) system diagram, (**b**) physical picture of scramjet model.
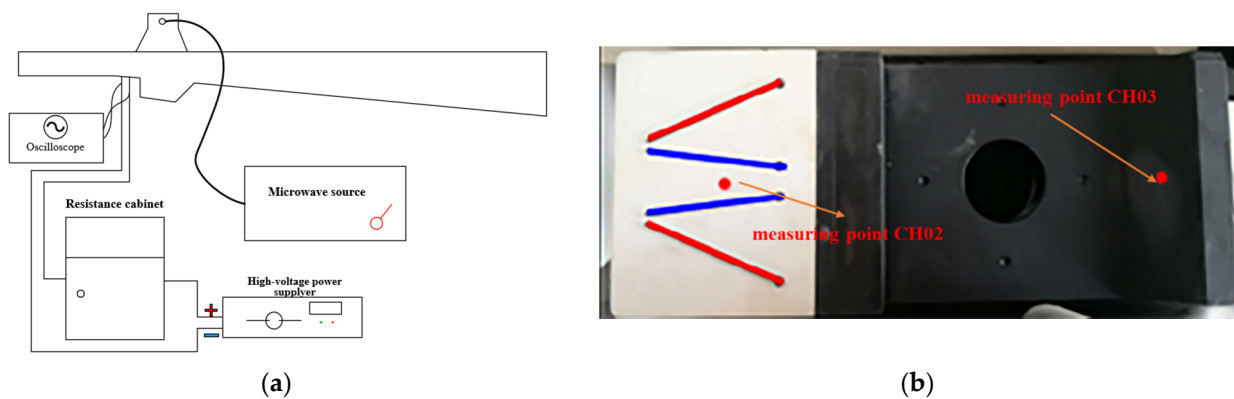

Figure 5. (**a**) Microwave and gliding arc facility diagram and scramjet model. (**b**) Electrode and cavity model.

There were two sets of electrodes in the combustion chamber that were located in the front of the cavity, as shown in Figure 5b. The electrode was powered by a high-voltage power supply with a maximum voltage of 10.0 kV and a current of 1.0 A. Protective resistors with resistance of 15 kΩ were installed between the power supply and the electrode.

The wall pressure was measured on the upper walls of the combustor using a DTC Initium ESP-32HD electronic pressure scanning module with a 100 psi range. High-frequency pressure-measuring points were arranged at the pressure-measuring points CH02 and CH03 using a KULITE XTEL high-frequency pressure sensor, as shown in Figure 5b.

The CH* observation windows were placed at the cavity. A high-speed camera was used in the experiment. The image of the 431 nm band could be captured directly by the high-speed camera with a filter; that is, the luminous intensity of CH* in the combustion area. The wavelength of the filter was 430 ± 15 nm and the peak transmittance was 0.882. We used a Phantom V1612 high-speed camera in the experiment, with a maximum resolution of 1280×800 and an actual use resolution of 512×256, and the experimental exposure time was 10 μs.

Figure 6 shows the time sequence of the experiment. The effective experimental time was from 2 s to 4 s. The heater preparation time was before 0 s, and the ignition time was from 0 s to 2 s. The experimental case of the scramjet is shown in Table 3.
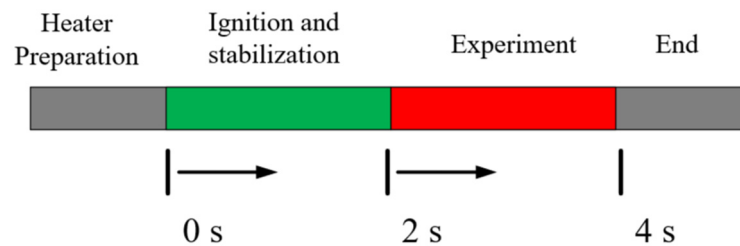

Figure 6. Experimental timescale.

Table 3. Experimental parameters.

| Case | Equivalence Ratio | Microwave Power | | | Gliding Arc |
		Peak	Repeated Frequency	Duty Cycle	
A1	0.15		Off		Off
A2	0.15	500 W	Off	100%	Off
A3	0.15	700 W	Off	100%	Off
B1	0.15	1 kW	10 kHz	10%	8 kV
B2	0.18		Off		Off
B3	0.18	1 kW	10 kHz	10%	8 kV

2.4. Microwave Feed Design and Intensity Calculation

In order to characterize the distribution and the propagation characteristics of the electromagnetic field in the combustion chamber after the addition of microwaves, HFSS simulation software was used to simulate the electromagnetic field inside the scramjet model.

Figure 7 shows the structure of the microwave computing domain. The green part in Figure 7 represents the quartz glass. The upper side of the glass was the horn antenna. The ideal conductor boundary condition was used on the wall, the radiation boundary condition was used at the entrance and the exit, and the microwave feed position was above the cavity. The frequency-domain finite element analysis method was used in the calculation. The main excitation frequency was 2.45 GHz.
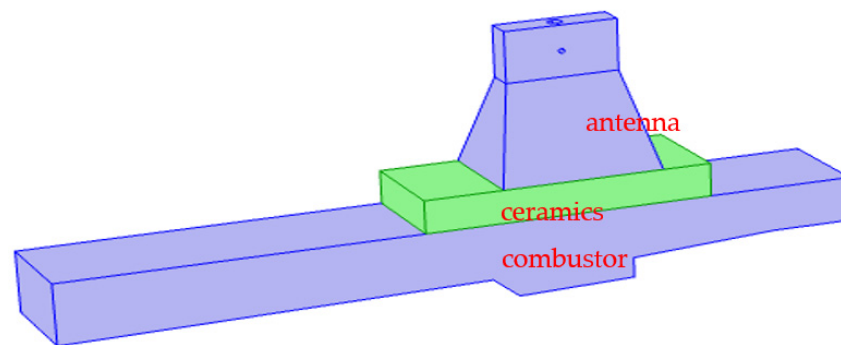
Figure 7. HFSS simulation model.

Figure 8 shows the calculation results of electric field intensity distribution at the dominant frequency of 2.45 GHz. It can be seen that the electric field was mainly distributed in the cavity area of the combustion chamber. In other words, after the 2.45 GHz microwaves were applied, the power was not transferred to both ends but, rather, gathered in the combustor, which was beneficial for improving the electric field energy in the local area. Based on the distribution of the electric field, a concentrated high-electric-field area was formed in the center of the flow channel, and the maximum intensity was no more than 1000 V/m, which was lower than the breakdown voltage. The electric field intensity had a polarization direction that was perpendicular to the flow direction and pointed to one of the side walls.
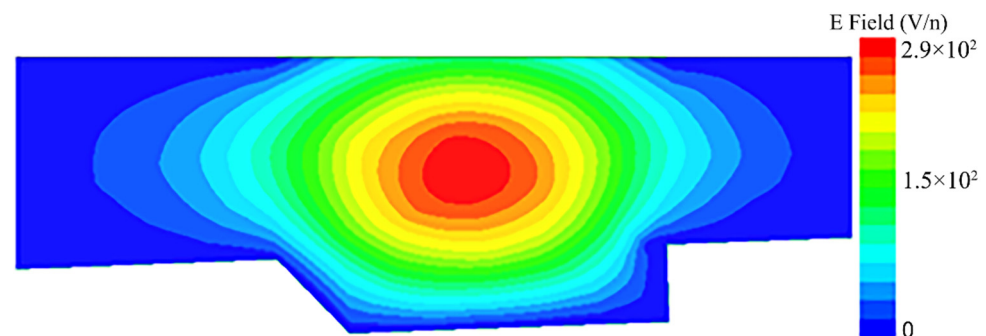

Figure 8. Simulation result of the cavity electric field.

2.5. Discharge Characteristics of the Gliding Arc in Supersonic Flow

When the voltage acted on the electrode, it was broken down at the nearest position of the two electrodes to form an arc. Then, due to the effect of the air flow, the arc glided and elongated along the electrode to form a gliding arc. When the current could not support the length of the arc, the arc broke and, at the same time, another arc reformed at the starting position, so the cycle repeated. Additionally, because the length of the arc changed the arc resistance, the periodic law of voltage appeared at the electrodes. The cycle characteristics of the gliding arc can be found in reference [44].

As shown in Figure 5b, the supersonic flow direction was from left to right, and the starting position of the gliding arc was on the left side of the electrodes, followed by expansion. When the current could not support the arc length, the arc broke and formed again on the left side of the electrode. Figure 9 shows the periodic characteristics of the voltage and current of the electrodes. In Figure 9, the high and low points of the voltage represent the generation and expansion of the gliding arc, respectively, and the current was opposite to the voltage trend. The voltage period was ~8 μs, and the frequency was ~125 kHz. The average arc power was ~102.8 W, the maximum instantaneous power was 3934.9 W, and the minimum was 0 W.
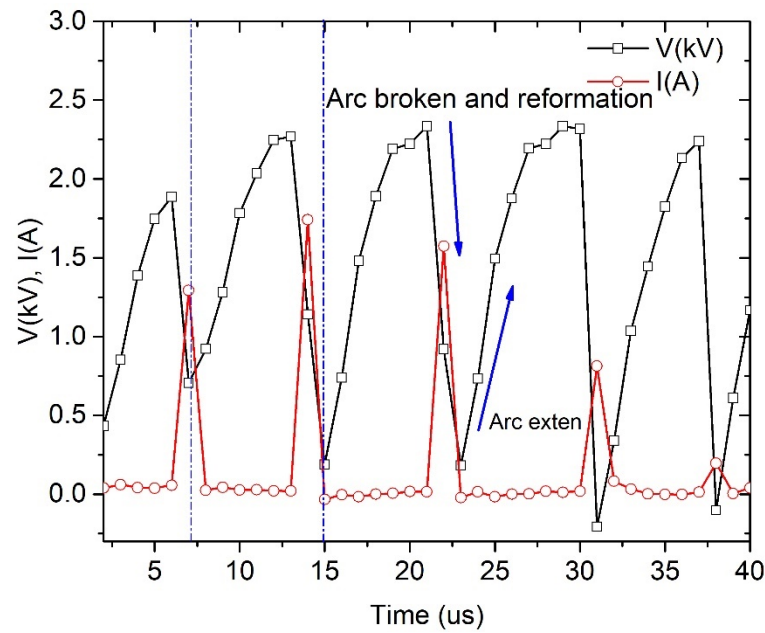
Figure 9. Gliding arc voltage and current period characteristics.

2.6. Method of OH Rotation and Vibration Temperature Analysis

The energy level transition produced the corresponding wavelength spectrum in a diatomic molecule. The spectral intensity $I_{v''J''}^{v'J'}$ represents the energy emitted by the source in a unit of time, as shown in Formula (1) [45].

$$I_{v''J''}^{v'J'} = \frac{64\pi^4 c \cdot P_{v''J''}^{v'J'} \cdot S_{J''}^{J'} \left(v_{v''J''}^{v'J'}\right)^4}{3} \frac{N_0 g_e'}{Q_e Q_v Q_r} exp\left(-\frac{E_e}{kT_e}\right) exp\left(-\frac{E_v}{kT_v}\right) exp\left(-\frac{E_r}{kT_r}\right) \quad (1)$$

where $P_{v''J''}^{v'J'}$, $S_{J''}^{J'}$, $v_{v''J''}^{v'J'}$, g_e', E_e, E_v, and E_r were determined by the molecular structure—that is to say, they were known quantities for OH. Therefore, for certain molecules or radicals, the spectral intensity $I_{v''J''}^{v'J'}$ was only related to the electron temperature T_e, vibration temperature T_v, and rotation temperature T_r. A detailed calculation method can be found in reference [45].

For OH ($A^2\Sigma^+ \rightarrow B^2\Pi_\gamma$), there were four spectral intensity peaks (G_0, G_1, G_2, and G_3), corresponding to different energy level transitions, in the range of 305–312 nm. If the peak intensity of G_0 was defined as 1000, the peak intensities of G_1, G_2, and G_3 gradually increased with the increase in the rotation temperature and the vibration temperature, which was an important judgment basis for the measurement of the rotational temperature and the vibration temperature with the emission spectrum of the OH free radical electron band ($A^2\Sigma^+ \rightarrow B^2\Pi_\gamma$).

In this study, the rotational and vibrational temperatures of the OH radicals were measured by simulating the experimental spectra with LIFBASE software, while considering of the collisional broadening and Doppler broadening in a Bunsen flame.

3. Results

3.1. Analysis of Flame Emission Spectra Influenced by Arc Plasma

As shown in Figures 10 and 11, from spectral emission lines in the UV–Vis wavelength range, molecular radicals such as OH, N_2, CH*, and C_2 appeared in the flame, compared with a flame without plasma. The line intensity of free radicals such as OH, N_2, CH*, and C_2 increased with the increase in the arc power.
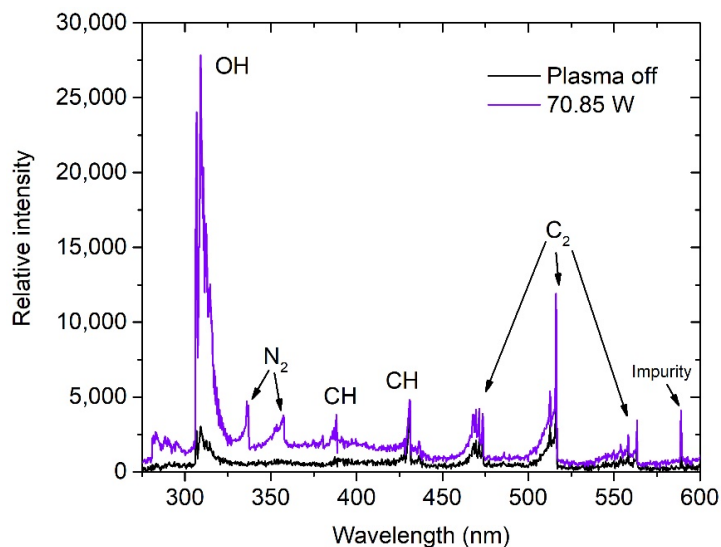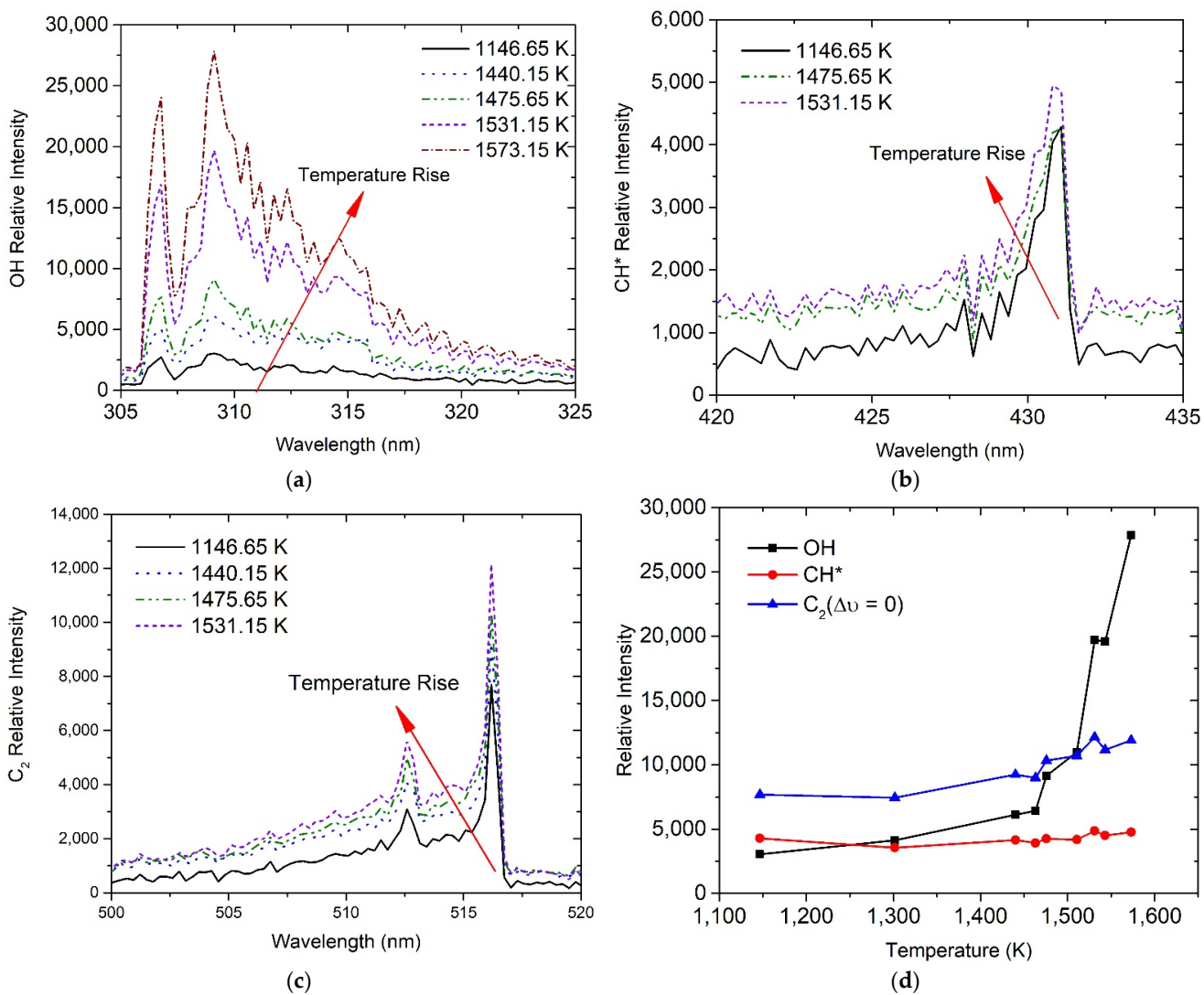
Figure 10. Flame spectrum with arc power.

Figure 11. Free radical luminescence intensity with flame temperature: (**a**) OH; (**b**) CH; (**c**) C$_2$ $d^3\Pi_g \rightarrow a^3\Pi_u$ ($\Delta v = 0$). (**d**) Free radical luminescence intensity increased with temperature.

In order to show the free radical luminescence intensity more clearly, Figure 11 displays the radical emission bands. The relative intensity of the OH (309.1 nm, $A^2\Sigma^+ \rightarrow B^2\Pi_\gamma$) radical spectrum increased rapidly, and the maximum increased by more than 10-fold compared to having the plasma off, while the other radicals (CH* 431 nm, C_2 516.18 nm) had a slow increase. The relative intensity of the OH (309.1 nm, $A^2\Sigma^+ \rightarrow B^2\Pi_\gamma$) radical spectrum was weaker than that of the C_2 Swan band ($d^3\Pi_g \rightarrow a^3\Pi_\mu$ ($\Delta\upsilon = 0$)) in the flame without plasma, but it became much stronger when the plasma was on, as can be seen from Figure 11d. The luminescence intensity could represent the amount of free radicals, so the DC arc caused the combustion to produce more OH without generating more of other free radicals, such as C_2 and CH*, demonstrating that the combustion reaction path was transitioned.

The arc discharge in the air could generate O (777.6 nm) atoms because of the electronic collision [46], as shown in Figure 12.
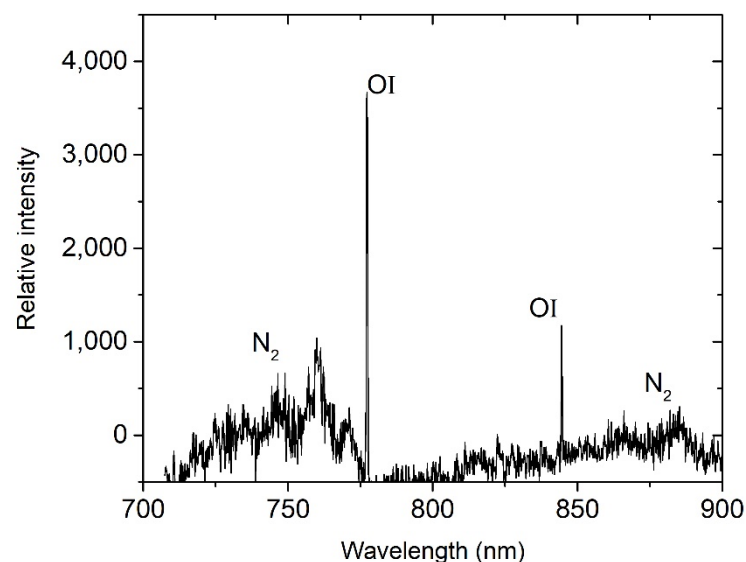
$$e + O_2 \rightarrow O + O(1D) \tag{2}$$

$$e + O_2^+ \rightarrow O + O \tag{3}$$

$$H + O_2 \rightarrow OH + O \tag{4}$$

Figure 12. Infrared spectrum of arc discharge in the air.

The oxygen atoms could react directly with ethylene to produce CH_xO.

$$C_2H_4 + O \rightarrow CH_xO \tag{5}$$

Therefore, the effect of arc plasma on the combustion was not only a thermal effect, but also an ion dynamic effect.

3.2. Analysis of OH Rotation and Vibration Temperature Influenced by Arc Plasma

After setting the OH ($A^2\Sigma \rightarrow X^2\Pi$) transition 0-0 band maximum intensity (G_0) to 1000, the spectral structure was observed, as shown in Figure 13. There was no significant difference between the OH with and without plasma, meaning that the plasma did not change the rotation or vibration temperature of the OH radical, but did increase the OH quantity.

The rotational and vibrational temperatures of the OH radicals were measured by simulating the experimental spectra with LIFBASE software, with consideration of the collisional broadening and the Doppler broadening in the Bunsen flame with 70.85 W plasma, which showed T_{vib} = 5000 K and T_{rot} = 3900 K.
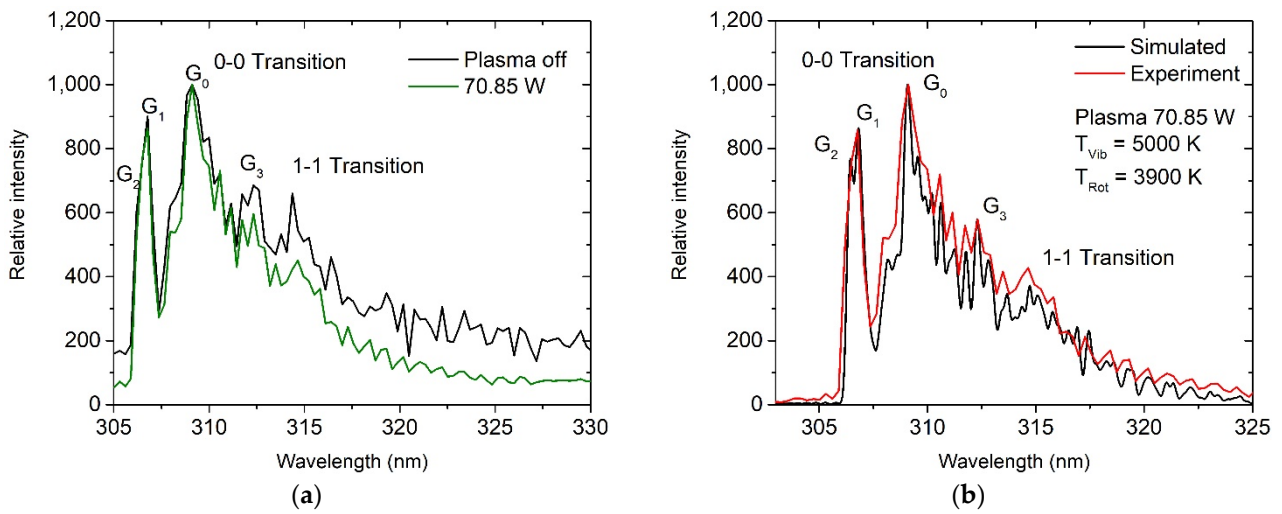
Figure 13. (**a**) OH spectrum with and without plasma; (**b**) OH rotation and vibration temperature with 70.85 W plasma.

3.3. Spectral Analysis of Flames Affected by Microwaves

Figure 14 shows the spectra of near-ultraviolet and visible light with different microwave powers. It can be seen from the figures that there was no obvious change in the types of main free radicals. OH (0-0), CH* (0-0), C_2 (1-0), C_2 (0-0), and C_2 (0-1) were found in the flame. In order to study the effect of the microwaves on different free radicals, each group was observed separately in Figure 15.
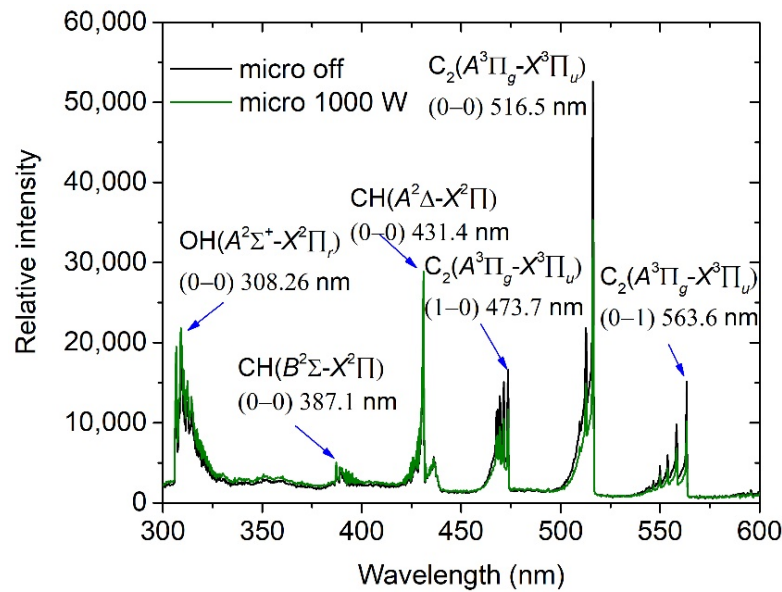

Figure 14. Microwave-influenced ethylene flame emission spectra.

Figure 15 shows the changes in the OH (a) and CH* (b) radical luminescence spectra after adding microwaves. It can be seen that the OH spectral intensity became stronger after adding microwaves. However, in the range of 100–800 W, the increase was not obvious, but there was a large increase after the power went up to 1000 W. Additionally, the intensity of CH* increased slightly after adding microwaves.

As shown in Figure 16, the C_2 group had three emission bands in the visible range. It was found that the intensity decreased with the increase in the microwave power, and decreased significantly after the microwave power went up to 1000 W.
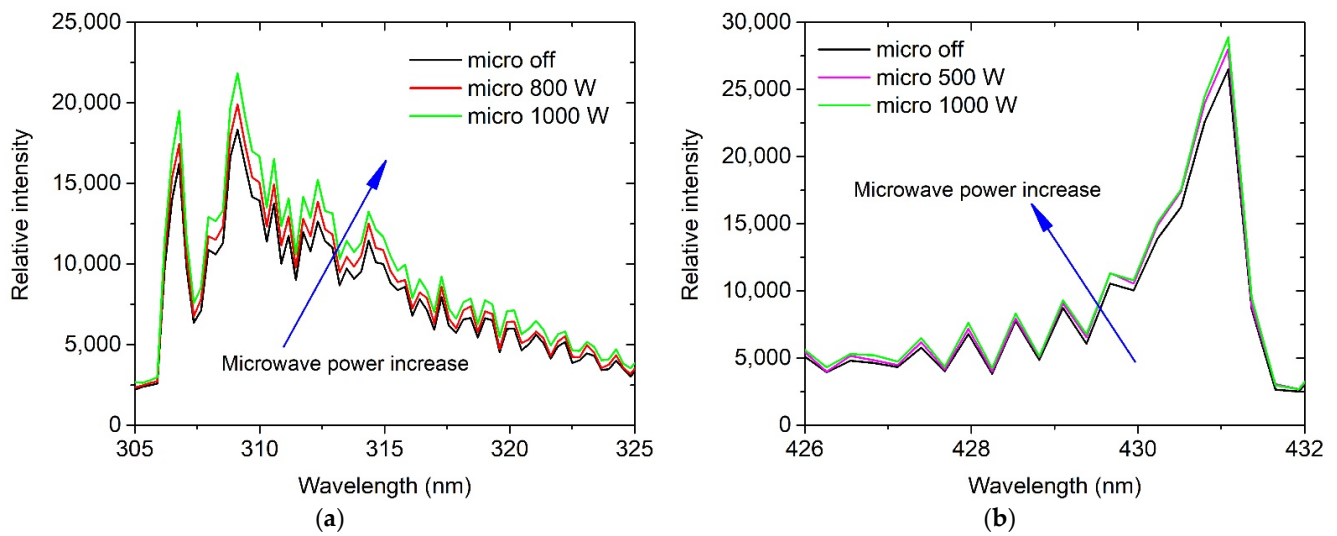
Figure 15. Microwave-influenced ethylene flame emission spectra: OH and CH*, (**a**) OH luminescence spectra, (**b**) CH* luminescence spectra.
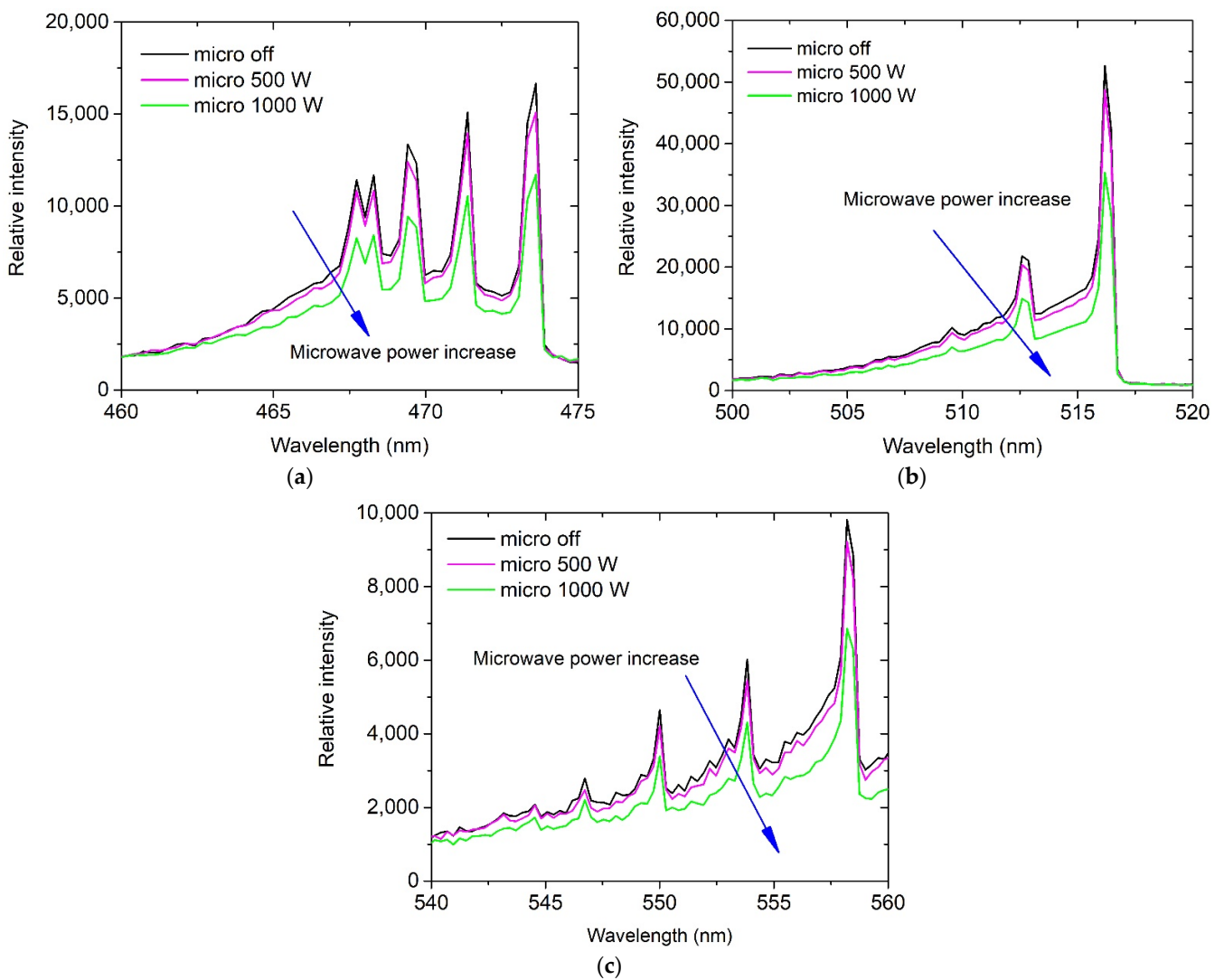

Figure 16. Microwave-influenced ethylene flame (**a**) C_2 (1-0), (**b**) C_2 (0-0), and (**c**) C_2 (0-1) emission spectra.

In order to show the free radical luminescence intensity trend more clearly, as shown in Figure 17, the OH increased quasi-linearly below 800 W, and suddenly increased when the power reached 1000 W. In contrast, the luminescence intensity of the C_2 decreased sharply. Obviously, after adding microwaves and reaching a certain power, the chemical reaction path changed, showing that the power of 1000 W was the threshold of the influence of microwaves on the flame. When the microwave power was lower than 1000 W or 800 W, it could affect the flame, but not obviously; with the continuous increase in power, an obvious effect was produced.
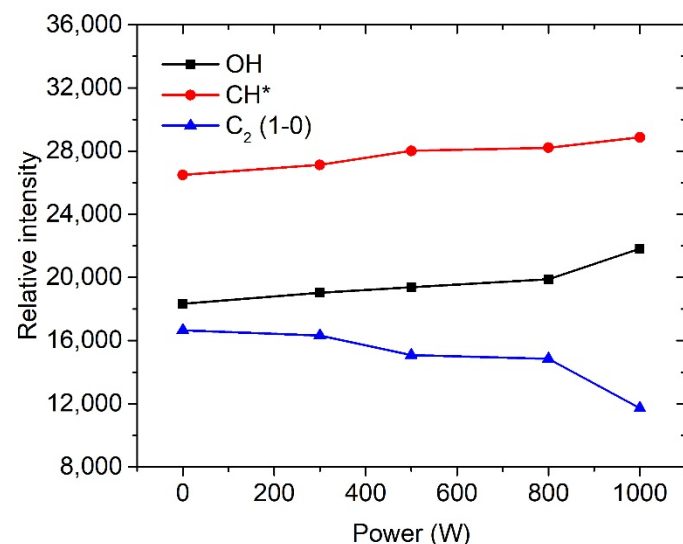

Figure 17. Radiation spectrum of free radicals with power.

3.4. Pressure Characteristics of Scramjet Influenced by Plasma

Figure 18 shows the pressure history (1 bar = 100 kPa) measured by the high-frequency pressure sensor at the rear edge of the cavity (CH03 in Figure 5b).
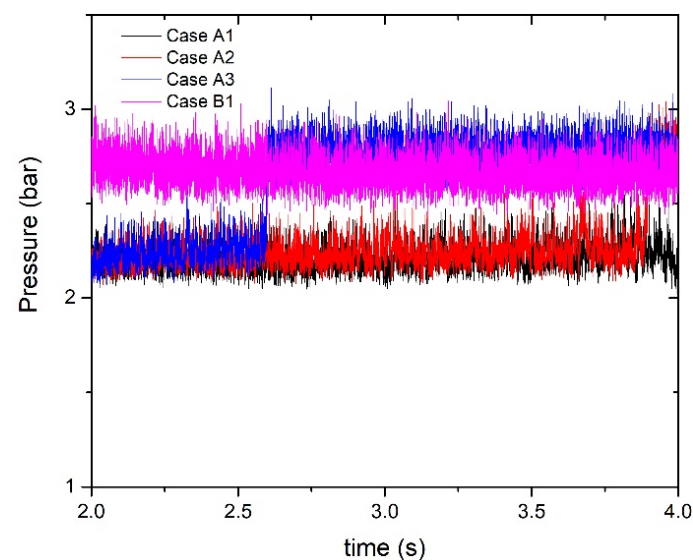

Figure 18. Cavity pressure history at different plasma powers.

There was almost no difference in pressure at the initial stable time of combustion. As time went on, the pressure rose sharply in the case of plasma assistance, and the position of the rising pressure point moved forward with the increase in the microwave power, such as in cases A1–A3. In case B1, the combustion pressure was high at the initial time due to

the microwave-enhanced gliding arc plasma, which indicated that the combined effect of the plasma had a more significant combustion assistance effect.

The equivalence ratio was increased to 0.18, and attention was paid to the pressure at CH02 (Figure 5), as shown in Figure 19. The shock train moved forward and crossed the pressure-measuring point with the influence of the plasma, resulting in an increase in the pressure at that position (CH02). In general, the pressure oscillated back and forth at the CH02 measuring point, and the addition of plasma made it easier for the pressure to stabilize upstream of the measuring point.
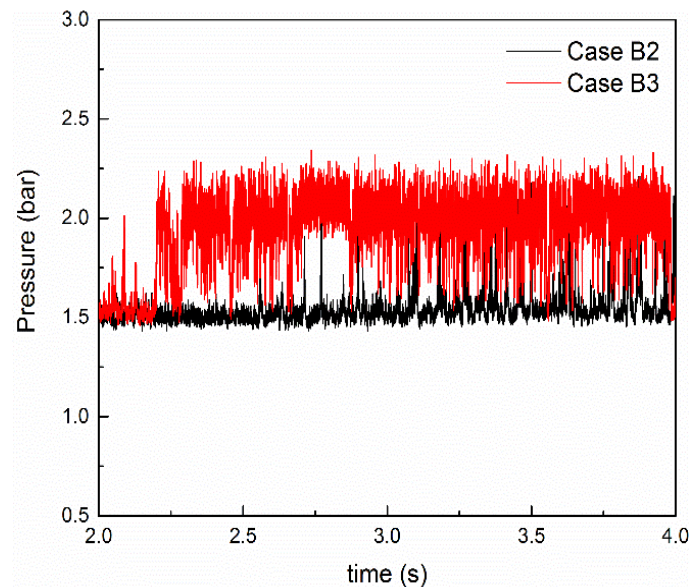
Figure 19. History of cavity pressure point CH02 while $\Phi = 0.18$.

The pressure not only represented combustion intensity, but also reflected the structure and position of the flame. The combustion mode was defined as mode A with low pressure and mode B after the increase in pressure.

Figure 20 shows the pressure along the path for different microwave powers at mode B. It was found that the rising point of the mode B pressure in the isolator was in front of that in mode A, and the pressure peak areas were relatively concentrated.
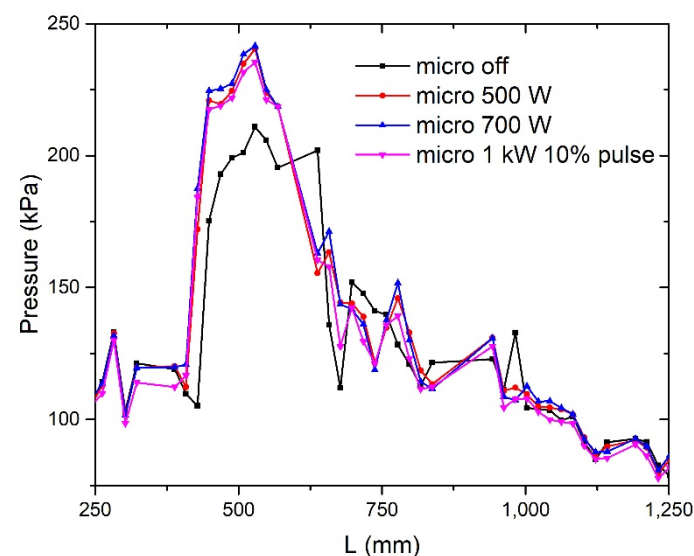
Figure 20. Pressure along the combustor path at different powers.

3.5. Characteristics of Average Flame Structure Affected by Plasma

One hundred images were extracted from modes A or B for the gray average, as shown in the left-hand side of Figure 21. The pseudo-color images are shown on the right-hand side of the figure.
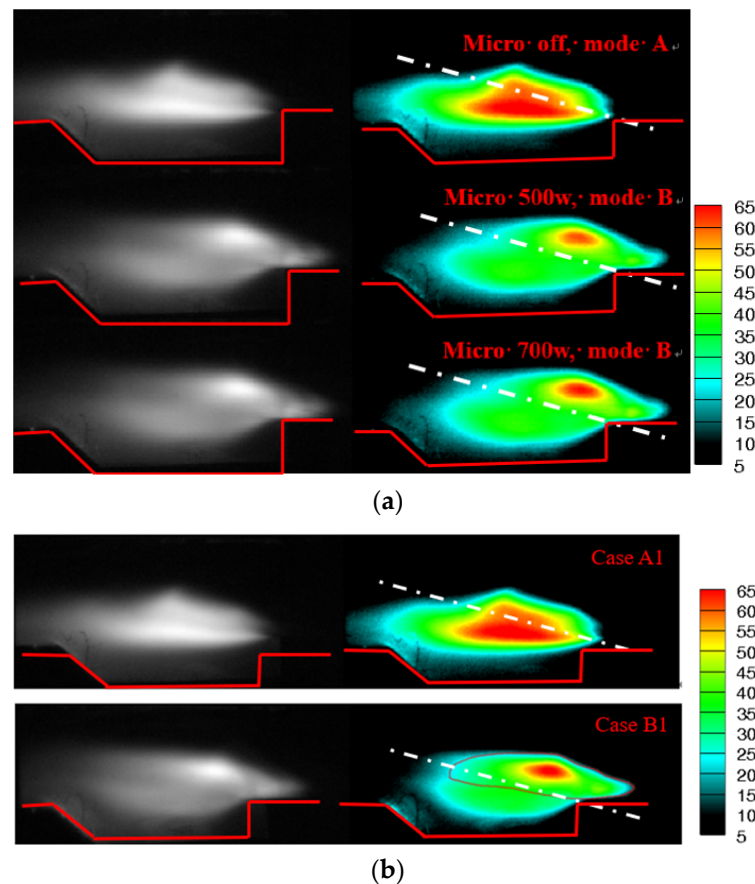

(a)

(b)

Figure 21. Average CH* images of flame mode: original images (**left**); pseudo-color images (**right**), (**a**) results of microwave experiments, (**b**) results of microwave enhanced gliding arc experiments.

The flame area could be divided into two combustion areas according to the distribution of the shear layer in the cavity. The lower side of the white dotted line in the figure represents the main combustion area of the shear layer, while the upper side of the white dotted line represents the jet flame stabilization area. The significance of this division is mainly to analyze the changes in the flame structure caused by the plasma. After plasma was added, the flame's high-intensity region was transferred from the stable flame region of the cavity to the jet flame stabilization region, and the flame extended forward towards the front. The heat release area of the flame was larger, and the core of the strong heat release zone became smaller and more concentrated in the jet flame's stabilizing area, which caused the wall pressure to rise.

Similarly, when the equivalence ratio was 0.18, the flame structure changed greatly with the influence of plasma, as shown in Figure 22. The flame stabilized in two areas, without plasma, as shown by the yellow and red ellipse marks in Figure 22. The yellow marks could be regarded as the flame stabilization area formed by the jet, while the red mark could be regarded as the flame stabilization area formed by the cavity. With the influence of plasma, the two regions recombined, and almost all of the flame-stabilizing region of the jet was transferred to the recirculation region in front of the jet.
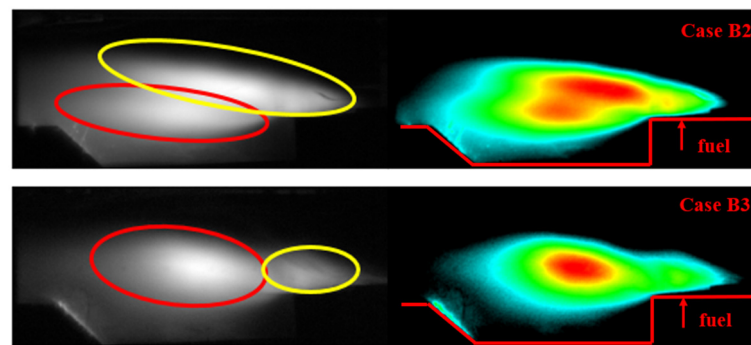
Figure 22. Average CH* images of flame mode while Φ = 0.18: original images (**left**); pseudo-color images (**right**).

In the supersonic flow, plasma was produced by the gliding arc, which was expanded by the microwaves and then acted on the flame [47]. Figure 23 shows the interaction between the plasma and the flame in the scramjet. Due to the effect of the plasma, the flame in the cavity was pushed forward, which made the jet-stabilized flame region develop forward, thus forming the flame structure shown in Figures 21 and 22.
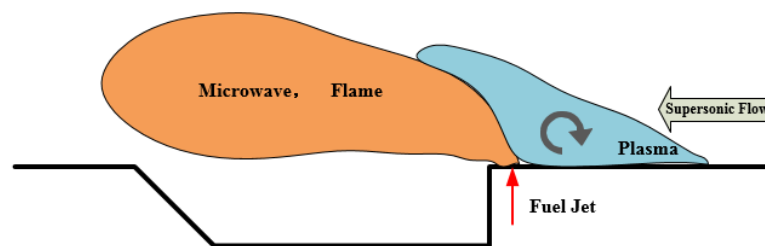

Figure 23. Schematic diagram of plasma and flame interaction.

4. Discussion

For the cavity combustion of a scramjet, the combustion become unstable during the modification process of scramjet mode and ramjet mode during aircraft acceleration or deceleration [12]. In this study, a plasma-assisted supersonic combustion method was proposed to modify the flame structure. The mechanism of microwave-extended gliding-arc-plasma-assisted combustion was studied and applied to a scramjet. The following conclusions can be drawn:

1. The arc plasma could increase the flame temperature in the power range of 0–70.85 W, and the temperature was not proportional to the arc power but, rather, to the current;
2. With the increase in the flame temperature, the concentration of OH radicals in the intermediate combustion increased ninefold at an arc power of 70.85 W, while the concentrations of CH* and C_2 did not change significantly;
3. The rotation temperature and vibration temperature of the OH radicals did not change with the increase in the emission intensity, which was assisted by arc plasma;
4. The intensity of OH and CH^* radical emission increased while the intensity of C_2 emission decreased with the action of the microwaves. However, in the limited energy range of the microwaves (<800 W), there was no typical change in the intensity of the radicals. Nevertheless, when the microwave power reached a certain point (800–1000 W), the effect became obvious. Therefore, the effect of the microwaves on the flame was an integral effect, and only when a certain value was reached could the microwaves play a significant role;
5. The microwave-enhanced gliding arc plasma changed the structure of the scramjet flame sharply with low power. The integral effect explained the relationship between the flame structure's abrupt increasing position and microwave power.

5. Conclusions

This study concentrated on the mechanism of plasma changing supersonic combustion mode. The effects of an arc and microwave on flames were studied experimentally. The current of the arc is the main parameter influencing combustion, as opposed to power. Plasma mainly affects OH radicals in flames, showing that the plasma shifts the combustion reaction path in the direction of OH participation. The effect of microwaves on the flame is an integral effect, which explains the flame structure's abrupt increase during the addition of plasma. However, the experiments in the paper had flaws, such as the microwave addition setup not being suitable, resulting in a waste of energy. In the future, the experimental technology should be optimized to supplement the flame trend affected by microwaves.

Author Contributions: Conceptualization, H.G. and Y.M.; methodology, Y.M.; writing—original draft preparation, Y.M.; writing—review and editing, F.C. All authors have read and agreed to the published version of the manuscript.

Conflicts of Interest: The authors declare no conflict of interest.

References

1. Billig, F.S. Research on Supersonic Combustion. *J. Propuls. Power* **1993**, *9*, 499–514. [CrossRef]
2. Ju, Y.G.; Sun, W.T. Plasma assisted combustion: Dynamics and chemistry. *Prog. Energy Combust. Sci.* **2015**, *48*, 21–83. [CrossRef]
3. Reddy, P.N.; Venkatasubbaiah, K. Numerical Investigations on Development of Scramjet Combustor. *J. Aerosp. Eng.* **2015**, *28*, 04014120. [CrossRef]
4. Dooley, S.; Won, S.H.; Heyne, J.; Farouk, T.I.; Ju, Y.G.; Dryer, F.L.; Kumar, K.; Hui, X.; Sung, C.J.; Wang, H.W.; et al. The experimental evaluation of a methodology for surrogate fuel formulation to emulate gas phase combustion kinetic phenomena. *Combust. Flame* **2012**, *159*, 1444–1466. [CrossRef]
5. Zhu, S.-H.; Xu, X. Experimental Study on Flame Transition in a Two-Stage Struts Dual-Mode Scramjet. *J. Aerosp. Eng.* **2017**, *30*, 06017002. [CrossRef]
6. Aradag, S.; Gelisli, K.A.; Yaldir, E.C. Effects of Active and Passive Control Techniques on Mach 1.5 Cavity Flow Dynamics. *Int. J. Aerosp. Eng.* **2017**, *2017*, 1–24. [CrossRef]
7. Zhu, S.; Xu, X.; Ji, P. Flame Stabilization and Propagation in Dual-Mode Scramjet with Staged-Strut Injectors. *AIAA J.* **2017**, *55*, 171–179. [CrossRef]
8. Yan, Z.; Shaohua, Z.; Bing, C.; Xu, X. Hysteresis of mode transition in a dual-struts based scramjet. *Acta Astronaut.* **2016**, *128*, 147–159. [CrossRef]
9. Zhu, S.; Xu, X.; Yang, Q.; Jin, Y. Intermittent back-flash phenomenon of supersonic combustion in the staged-strut scramjet engine. *Aerosp. Sci. Technol.* **2018**, *79*, 70–74. [CrossRef]
10. Zhang, J.; Chang, J.; Ma, J.; Zhang, C.; Bao, W. Investigation of flame establishment and stabilization mechanism in a kerosene fueled supersonic combustor equipped with a thin strut. *Aerosp. Sci. Technol.* **2017**, *70*, 152–160. [CrossRef]
11. Masumoto, R.; Tomioka, S.; Kudo, K.; Murakami, A.; Kato, K.; Yamasaki, H. Experimental Study on Combustion Modes in a Supersonic Combustor. *J. Propuls. Power* **2011**, *27*, 346–355. [CrossRef]
12. Meng, Y.; Gu, H.; Zhuang, J.; Sun, W.; Gao, Z.; Lian, H.; Yue, L.; Chang, X. Experimental study of mode transition characteristics of a cavity-based scramjet combustor during acceleration. *Aerosp. Sci. Technol.* **2019**, *93*, 105316. [CrossRef]
13. Meng, Y.; Gu, H.; Zhang, X. Experimental Study of Kerosene Ignition and Flame Stabilization in a Supersonic Combustor. *Int. J. Turbo Jet-Engines* **2019**. [CrossRef]
14. Talati, H.; Aliakbari, K.; Ebrahimi-Moghadam, A.; Khoshbakht Farokhad, H.; Eskandary Nasrabad, A. Optimal design and analysis of a novel variable-length intake manifold on a four-cylinder gasoline engine. *Appl. Therm. Eng.* **2022**, *200*, 117631. [CrossRef]
15. Ebrahimi-Moghadam, A.; Ildarabadi, P.; Aliakbari, K.; Fadaee, F. Sensitivity analysis and multi-objective optimization of energy consumption and thermal comfort by using interior light shelves in residential buildings. *Renew. Energy* **2020**, *159*, 736–755. [CrossRef]
16. Ebrahimi-Moghadam, A.; Moghadam, A.J.; Farzaneh-Gord, M.; Aliakbari, K. Proposal and assessment of a novel combined heat and power system: Energy, exergy, environmental and economic analysis. *Energy Convers. Manag.* **2020**, *204*, 112307. [CrossRef]
17. Ju, Y.; Lefkowitz, J.K.; Reuter, C.B.; Won, S.H.; Yang, X.; Yang, S.; Sun, W.; Jiang, Z.; Chen, Q. Plasma assisted low temperature combustion. *Plasma Chem. Plasma Process.* **2016**, *36*, 85–105. [CrossRef]

18. Ju, Y.G.; Sun, W.T. Plasma assisted combustion: Progress, challenges, and opportunities. *Combust. Flame* **2015**, *162*, 529–532. [CrossRef]

19. Starikovskiy, A.; Aleksandrov, N. Plasma-assisted ignition and combustion. *Prog. Energy Combust. Sci.* **2013**, *39*, 61–110. [CrossRef]

20. Shahrbabaki, A.N.; Bazazzadeh, M.; Khoshkhoo, R.; Páscoa, J.C. Investigation on Supersonic Flow Control Using Nanosecond Dielectric Barrier Discharge Plasma Actuators. *Int. J. Aerosp. Eng.* **2021**, *2021*, 1–14. [CrossRef]

21. Li, X.; Yang, L.; Peng, J.; Yu, X.; Liang, J.; Sun, R. Cavity ignition of liquid kerosene in supersonic flow with a laser-induced plasma. *Opt. Express* **2016**, *24*, 25362. [CrossRef] [PubMed]

22. An, B.; Wang, Z.; Yang, L.; Li, X.; Zhu, J. Experimental investigation on the impacts of ignition energy and position on ignition processes in supersonic flows by laser induced plasma. *Acta Astronaut.* **2017**, *137*, 444–449. [CrossRef]

23. Zhong, H.; Mao, X.; Rousso, A.C.; Patrick, C.L.; Yan, C.; Xu, W.; Chen, Q.; Wysocki, G.; Ju, Y. Kinetic study of plasma-assisted n-dodecane/O_2/N_2 pyrolysis and oxidation in a nanosecond-pulsed discharge. *Proc. Combust. Inst.* **2020**, *38*, 6521–6531. [CrossRef]

24. Zhao, B.-b.; Chen, G.-C.; He, L.-M.; Jin, T.; Jing, B. Experimental Investigation of Plasma Jet Ignition Characteristics in Kerosene-Air Mixtures. *J. Aerosp. Eng.* **2020**, *33*, 04019113. [CrossRef]

25. Li, F.; Yu, X.-L.; Tong, Y.-G.; Shen, Y.; Chen, J.; Chen, L.-H.; Chang, X.-Y. Plasma-assisted ignition for a kerosene fueled scramjet at Mach 1.8. *Aerosp. Sci. Technol.* **2013**, *28*, 72–78. [CrossRef]

26. Cai, Z.; Zhu, J.; Sun, M.; Wang, Z. Spark-enhanced ignition and flame stabilization in an ethylene-fueled scramjet combustor with a rear-wall-expansion geometry. *Exp. Therm. Fluid Sci.* **2018**, *92*, 306–313. [CrossRef]

27. Feng, R.; Li, J.; Wu, Y.; Zhu, J.; Song, X.; Li, X. Experimental investigation on gliding arc discharge plasma ignition and flame stabilization in scramjet combustor. *Aerosp. Sci. Technol.* **2018**, *79*, 145–153. [CrossRef]

28. Jaggers, H.C.; Vonengel, A. Effect of electric fields on burning velocity of various flames. *Combust. Flame* **1971**, *16*, 275–285. [CrossRef]

29. Shinohara, K.; Takada, N.; Sasaki, K. Enhancement of burning velocity in premixed burner flame by irradiating microwave power. *J. Phys. D Appl. Phys.* **2009**, *42*, 182008. [CrossRef]

30. Stockman, E.S.; Zaidi, S.H.; Miles, R.B.; Carter, C.D.; Ryan, M.D. Measurements of combustion properties in a microwave enhanced flame. *Combust. Flame* **2009**, *156*, 1453–1461. [CrossRef]

31. Michael, J.B.; Chng, T.L.; Miles, R.B. Sustained propagation of ultra-lean methane/air flames with pulsed microwave energy deposition. *Combust. Flame* **2013**, *160*, 796–807. [CrossRef]

32. Ombrello, T.; Won, S.H.; Ju, Y.G.; Williams, S. Flame propagation enhancement by plasma excitation of oxygen. Part II: Effects of $O_2(a^1\Delta_g)$. *Combust. Flame* **2010**, *157*, 1916–1928. [CrossRef]

33. Khodataev, K.V. Microwave discharges and possible applications in aerospace technologies. *J. Propuls. Power* **2008**, *24*, 962–972. [CrossRef]

34. Baurov, A.Y.; Shibkova, L.V.; Shibkov, V.M.; Kopyl, P.V.; Surkont, O.S. External combustion of high-speed multicomponent hydrocarbon-air flow under conditions of low-temperature plasma. *Mosc. Univ. Phys. Bull.* **2013**, *68*, 293–298. [CrossRef]

35. Shibkov, V.M.; Shibkova, L.V.; Karachev, A.A.; Kopyl, P.V.; Surkont, O.S. The spatial-temporal evolution of combustion under conditions of low temperature discharge plasma of liquid alcohol injected into an air stream. *Mosc. Univ. Phys. Bull.* **2012**, *67*, 138–142. [CrossRef]

36. Shibkov, V.M.; Shibkova, L.V.; Gromov, V.G.; Karachev, A.A.; Konstantinovskii, R.S. Influence of surface microwave discharge on ignition of high-speed propane-air flows. *High Temp.* **2011**, *49*, 155–167. [CrossRef]

37. Shibkov, V.M.; Shibkova, L.V. Parameters of the flame due to surface-microwave discharge-initiated inflammation of thin alcohol films. *Tech. Phys.* **2010**, *55*, 58–65. [CrossRef]

38. Babushok, V.I.; DeLucia, F.C.; Gottfried, J.L.; Munson, C.A.; Miziolek, A.W. Double pulse laser ablation and plasma: Laser induced breakdown spectroscopy signal enhancement. *Spectrochim. Acta Part B At. Spectrosc.* **2006**, *61*, 999–1014. [CrossRef]

39. Michael, J.B.; Dogariu, A.; Shneider, M.N.; Miles, R.B. Subcritical microwave coupling to femtosecond and picosecond laser ionization for localized, multipoint ignition of methane/air mixtures. *J. Appl. Phys.* **2010**, *108*, 093308. [CrossRef]

40. Wolk, B.; DeFilippo, A.; Chen, J.-Y.; Dibble, R.; Nishiyama, A.; Ikeda, Y. Enhancement of flame development by microwave-assisted spark ignition in constant volume combustion chamber. *Combust. Flame* **2013**, *160*, 1225–1234. [CrossRef]

41. Ikeda, Y.; Nishiyama, A.; Kaneko, M. Microwave Enhanced Ignition Process for Fuel Mixture at Elevated Pressure of 1MPa. In Proceedings of the 47th AIAA Aerospace Sciences Meeting Including the New Horizons Forum and Aerospace Exposition, Prlando, FL, USA, 5–8 January 2009. [CrossRef]

42. ElSabbagh, M.; Kado, S.; Ikeda, Y.; Sasaki, K. Measurements of Rotational Temperature and Density of Molecular Nitrogen in Spark-Plug Assisted Atmospheric-Pressure Microwave Discharges by Rotational Raman Scattering. *Jpn. J. Appl. Phys.* **2011**, *50*, 076101. [CrossRef]

43. Fridman, A.; Nester, S.; Kennedy, L.A.; Saveliev, A.; Mutaf-Yardimci, O. Gliding arc gas discharge. *Prog. Energy Combust. Sci.* **1999**, *25*, 211–231. [CrossRef]

44. Sun, Z.W.; Zhu, J.J.; Li, Z.S.; Alden, M.; Leipold, F.; Salewski, M.; Kusano, Y. Optical diagnostics of a gliding arc. *Opt. Express* **2013**, *21*, 6028–6044. [CrossRef] [PubMed]

45. Peng, Z.M.; Ding, Y.J.; Zhai, X.D.; Yang, Q.S.; Jiang, Z.L. Spectral Characteristics of CN Radical (B→X) and Its Application in Determination of Rotational and Vibrational Temperatures of Plasma. *Chin. Phys. Lett.* **2011**, *28*, 044703. [CrossRef]

46.   Fridman, A.A. *Plasma Chemistry*; Cambridge University Press: Cambridge, NY, USA, 2008; p. 978.
47.   Rao, X.; Hemawan, K.; Wichman, I.; Carter, C.; Grotjohn, T.; Asmussen, J.; Lee, T. Combustion dynamics for energetically enhanced flames using direct microwave energy coupling. *Proc. Combust. Inst.* **2011**, *33*, 3233–3240. [CrossRef]